

Development of a deep learning method for phase retrieval image enhancement in phase contrast microcomputed tomography

Xiao Fan Ding¹  | Xiaoman Duan¹  | Naitao Li¹  | Zahra Khoz²  | Fang-Xiang Wu^{1,2}  | Xiongbiao Chen^{1,2}  | Ning Zhu^{1,3,4} 

¹Division of Biomedical Engineering,
University of Saskatchewan, Saskatoon,
Canada

²Department of Mechanical Engineering,
University of Saskatchewan, Saskatoon,
Canada

³Department of Chemical and Biological
Engineering, University of Saskatchewan,
Saskatoon, Canada

⁴Science Division, Canadian Light Source
Inc., Saskatoon, Canada

Correspondence

Ning Zhu, Division of Biomedical
Engineering, University of Saskatchewan,
Saskatoon S7N 5A9, Canada.
Email: ning.zhu@lightsource.ca

Funding information

University of Saskatchewan Graduate
Scholarship, NSERC INSPIRE Graduate
Fellowship, Grant/Award Numbers:
RGPIN 06007-2019, RGPIN 06396-2019;
National Research Council

Abstract

Propagation-based imaging (one method of X-ray phase contrast imaging) with microcomputed tomography (PBI- μ CT) offers the potential to visualise low-density materials, such as soft tissues and hydrogel constructs, which are difficult to be identified by conventional absorption-based contrast μ CT. Conventional μ CT reconstruction produces edge-enhanced contrast (EEC) images which preserve sharp boundaries but are susceptible to noise and do not provide consistent grey value representation for the same material. Meanwhile, phase retrieval (PR) algorithms can convert edge enhanced contrast to area contrast to improve signal-to-noise ratio (SNR), and contrast-to-noise ratio (CNR) but usually results to over-smoothing, thus creating inaccuracies in quantitative analysis. To alleviate these problems, this study developed a deep learning-based method called edge view enhanced phase retrieval (EVEPR), by strategically integrating the complementary spatial features of denoised EEC and PR images, and further applied this method to segment the hydrogel constructs *in vivo* and *ex vivo*. EVEPR used paired denoised EEC and PR images to train a deep convolutional neural network (CNN) on a dataset-to-dataset basis. The CNN had been trained on important high-frequency details, for example, edges and boundaries from the EEC image and area contrast from PR images. The CNN predicted result showed enhanced area contrast beyond conventional PR algorithms while improving SNR and CNR. The enhanced CNR especially allowed for the image to be segmented with greater efficiency. EVEPR was applied to *in vitro* and *ex vivo* PBI- μ CT images of low-density hydrogel constructs. The enhanced visibility and consistency of hydrogel constructs was essential for segmenting such material which usually exhibit extremely poor contrast. The EVEPR images allowed for more accurate segmentation with reduced manual adjustments. The efficiency in segmentation allowed for the generation of a sizeable database of segmented

hydrogel scaffolds which were used in conventional data-driven segmentation applications. EVEPR was demonstrated to be a robust post-image processing method capable of significantly enhancing image quality by training a CNN on paired denoised EEC and PR images. This method not only addressed the common issues of over-smoothing and noise susceptibility in conventional PBI- μ CT image processing but also allowed for efficient and accurate *in vitro* and *ex vivo* image processing applications of low-density materials.

KEY WORDS

convolutional neural network, deep learning, image processing, microcomputed tomography, phase contrast imaging

1 | INTRODUCTION

Phase contrast microcomputed tomography (μ CT) is a useful method for visualising soft tissues and low-density materials. Unlike conventional absorption contrast μ CT, which relies on the attenuation of X-rays, phase contrast μ CT detects the phase shift caused by coherent X-rays passing through a material.^{1–3} Propagation-based imaging (PBI) with microcomputed tomography is a phase contrast method and can use synchrotron radiation as a coherent X-ray source to achieve a detectable phase contrast. A PBI image acquisition setup is illustrated in Figure 1A where a highly coherent X-ray beam from a synchrotron light source is propagated between the sample and detector. Figure 1B shows how edge enhanced contrast (EEC) and phase retrieval (PR) μ CT images are reconstructed from the PBI X-ray projection data.

Although the EEC can effectively show the sample's boundaries, it also introduces fringe artefacts⁴ and is sensitive to noise,^{5,6} resulting in EEC images not typically used for quantitative analysis, for example, segmentation.^{7,8} The susceptibility to noise could be alleviated by denoising methods such as wavelet-based denoising,⁹ non-local means denoising,^{10,11} or deep learning-based denoising.^{12–15} Denoising would maximise the edge enhancement but still does not quantitatively show the area of the different materials because the characteristic bright-dark bands along edges indicate that a material cannot be represented by a consistent grey value. Since the EEC seen in PBI is the second derivative of the phase shift,¹⁶ this led to the widespread use of PR algorithms which recover the phase shift imposed on the X-ray beam by the interacting material and produced images that were more suitable segmentation.^{4,17}

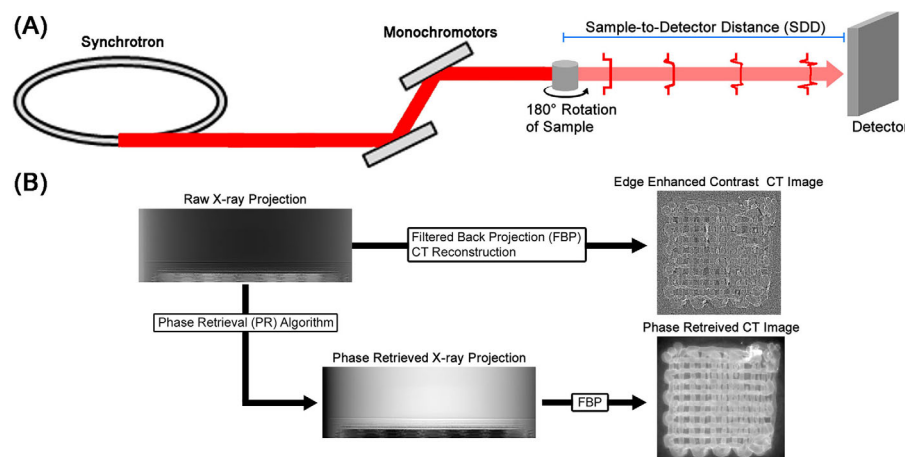


FIGURE 1 (A) Illustration of synchrotron radiation-based PBI and the effect of a low-density sample on the X-ray beam. The sample is a soft tissue like hydrogel construct. When a highly coherent X-ray beam interacts with the sample, it results in a phase-shift and a distortion of the X-ray wavefront, leading to intensity variations with increasing fringe visibility along the propagation direction. (B) The raw X-ray projection data can be directly reconstructed using filtered back projection (FBP) to obtain an edge enhanced contrast (EEC) μ CT image. Alternatively, the phase shift can be recovered through a phase retrieval (PR) algorithm before reconstructing with FBP to obtain a phase retrieved (PR) image.

There are many PR methods available for PBI, but there is a particular focus on non-iterative methods that do not require multiple intensity measurements.¹⁸ The common mathematical framework shared by different methods such as the Bronnikov method,¹⁹ phase-attenuation duality,²⁰ and transport of intensity (TIE)-based methods^{21,22} is that the algorithm represents the measured intensity at the imaging detector as a function. A forward Fourier transformation is applied to the function, the data is filtered in the frequency domain, and then an inverse Fourier transformation is applied followed by a phase extraction function to retrieve the phase information.¹⁸ In particular, the TIE-based methods offer a robust and practical phase retrieval solution for homogeneous objects with both computational efficiency and accuracy. This makes TIE appealing in scenarios where imaging and material properties are known such as the X-ray energy, SDD, effective pixel size, and delta-over-beta ratio (δ/β), the ratio of the real and imaginary components of the refractive index of the material interacting with the X-ray beam. However, TIE is a low-pass filter that smooths high-frequency image components which is beneficial in noise reduction but can also smooth edges.²³ Not only can the smoothing result in image artefacts, the TIE algorithms also do not suppress artefacts from more neighbouring materials that are more attenuating.²⁴

Given the challenges in quantitative analysis using both EEC and PR images, there is a need for enhancement methods capable of preserving image features. Deep convolutional neural networks (CNNs) have shown great promise for this with the U-Net architecture becoming widely adopted because of its capability in capturing spatial context.²⁵ While there exist better performing architectures,^{26–28} U-Net has prevailed with its ability to work with smaller datasets and being computationally inexpensive.²⁹ Trained CNNs have been used to learn the similar spatial information in paired images for denoising^{15,13} and image enhancement.³⁰ Thus, there is potential to similarly train a deep learning PR image enhancement model trained on paired EEC and PR images as both can be obtained in PBI.

In recent years, deep learning has impacted phase retrieval methods, some with application in PBI- μ CT.^{31,32} Among such developments, physics-driven, physics-informed, and domain-informed models offer greater capabilities by incorporating physical principles into designing the deep learning frameworks^{33,34} or by strategically training on data that is defined by the user's understanding of the foundational physics.^{35,36} Models like PhaseGAN, AutoPhase-NN, and DH-GAN have demonstrated improvements in image contrast, noise reduction, and computational efficiency but typically require a priori references for model training which limits

their general application.^{37–40} This study focuses on the development of a deep learning method, called edge view enhanced phase retrieval (EVEPR), that incorporates the physical principles in coherent X-ray interactions with matter in PBI- μ CT. By training on paired denoised EEC and PR images via a CNN, the network predicts results that has been trained on important high-frequency details, for example, edges and boundaries from the EEC image and area contrast from PR images and are used to enhance PR images beyond conventional PR algorithms. The proposed method uses paired images which can both be obtained from the same raw X-ray projection data and will not rely on a priori references and work on a dataset-to-dataset basis.

2 | MATERIALS AND METHODS

2.1 | Propagation-based imaging data acquisition

PBI scans were performed at the 05ID-2 beamline of Canadian Light Source (CLS).⁴¹ Each scan was performed using a 30 keV monochromatic beam which propagated along a 1.5 m sample-to-detector distance. An indirect detection method was used, consisting of a Hamamatsu AA-60 beam monitor (Hamamatsu Photonics K.K., Hamamatsu, Japan), a 500 μ m thick LuAG scintillator, and a Hamamatsu Orca Flash 4 camera (Hamamatsu Photonics K.K., Hamamatsu, Japan). The effective pixel size of the camera was 13 μ m with a field-of-view of 26.6 by 6.5 mm. Each raw dataset acquired 3000 X-ray projections as the sample was rotated over 180°.^{42,43} The raw X-ray projection data was subject to two image processing steps as shown in Figure 2: Figure 2A, the denoising step used the Noise2Inverse method after hyperparameter tuning on the EEC results¹³ and Figure 2B, a PR algorithm was applied to the X-ray projections, CT reconstruction, and training CNN based on paired denoised EEC and PR images which will be called the EVEPR step.

2.2 | Image processing steps

The denoising step (shown in Figure 2A) used the Noise2Inverse with the U-Net architecture. The choice in loss functions were determined through hyperparameter tuning^{13,30} with the results shown in Section 3.3. The original raw X-ray projection dataset was divided into two equal splits, that is, a raw dataset of 3000 projections was divided into two 1500 projection sub-datasets. The split datasets were reconstructed using filtered back projection (FBP) using ufo-toolkit⁴⁴ with Fourier wavelet-based ring

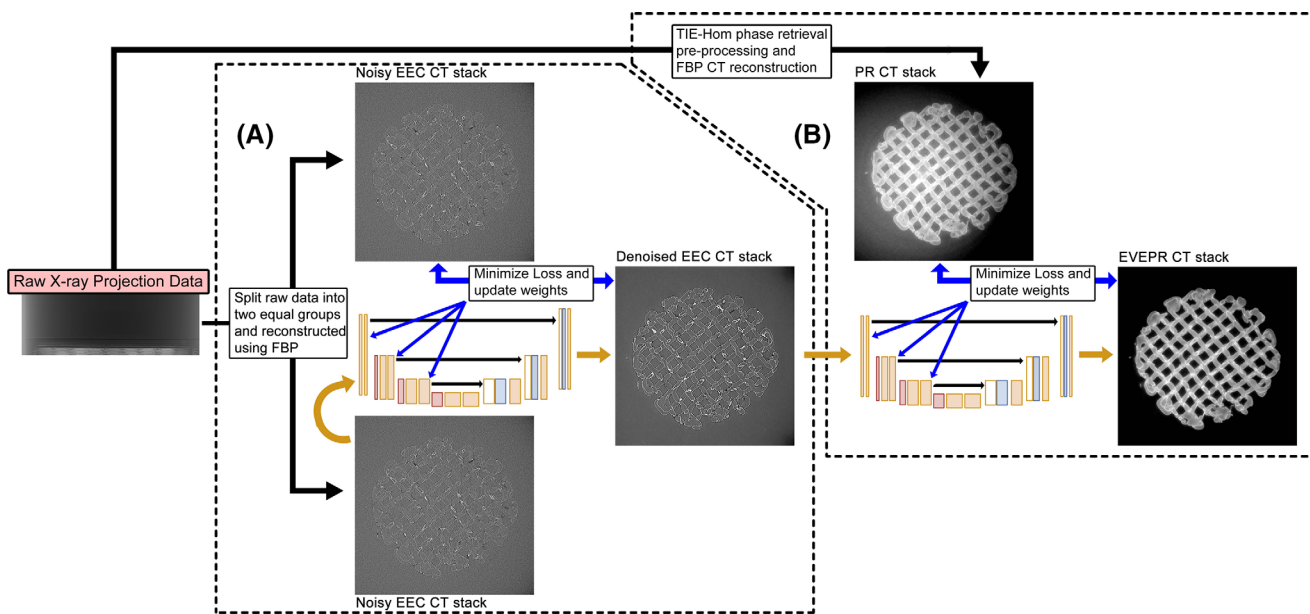


FIGURE 2 Flowchart of a phase retrieval image enhancement strategy by training a CNN with using denoised EEC and PR images. There are two main steps: (A) the denoising step and (B) the EVEPR step.

removal algorithms.⁴⁵ The two reconstructed μCT stacks, hereafter called noisy EEC images, exhibited the same EEC features but independent noise distributions because there was no overlap in raw data. The two noisy EEC image stacks served as the input and target for training the first CNN, which predicted a denoised EEC output that served as the input to the second CNN in the EVEPR step.

The EVEPR step (shown in Figure 2B) first used the TIE²¹ phase retrieval algorithm on the original raw X-ray projection dataset. The phase retrieved projections were reconstructed using FBP and Fourier wavelet-based ring removal. The reconstruction result, hereafter called the PR image, served as the target in the second CNN. The second CNN prediction, hereafter referred to as the EVEPR image, exhibited an enhanced area contrast over the conventional PR image as well as more consistent grey value. The improvement in SNR and CNR, which are formulated below as Equations (1) and (2).⁴⁶

$$\text{SNR} = \left| \frac{I_{\text{ROIForeground}}}{\sigma_{\text{ROIBackground}}} \right|, \quad (1)$$

$$\text{CNR} = \left| \frac{I_{\text{ROIForeground}} - I_{\text{ROIBackground}}}{\sigma_{\text{ROIBackground}}} \right|, \quad (2)$$

I_E and σ denote the average grey value and the standard deviation of an ROI, respectively. The foreground represents an ROI containing the objective samples (i.e., hydrogel construct) and the background represents an ROI of the same size excluding objective samples (i.e., the distilled water in which hydrogel construct is placed in when scanning).

Both the denoising and EVEPR steps were inspired by Noise2Noise. Overfitting is mitigated because using input and target training pairs with independent differences, that is, noise in the denoising step and complementary edge enhanced and area contrast in the EVEPR step, ensures that the CNN learns spatial information rather than memorising individual pixel intensities. In addition, finding an ideal loss function promotes generalisation, focusing on maintaining consistent image structure rather than overfitting to variations.

EVEPR can produce higher quality results by minimising the loss between the input and target, for example, denoised EEC and PR images, respectively. This is without an a priori reference and the expected improvement in SNR and CNR which should improve the ease of segmentation. Individual slices of the EVEPR image stack can be segmented by thresholding.⁴⁷ The full EVEPR image stack could then be segmented by a random-walk interpolation algorithm, for example, Biomedisa.⁴⁸ The segmentation accuracy could then be quantified by the Dice coefficient and Jaccard index using a manual segmentation as the ground truth.^{49,50} Both the Dice and Jaccard values are overlap tests that are widely used in segmentation analysis.⁵¹ The Jaccard index is more sensitive to discrepancies between the segmented volumes and can be more stringent when the overlap is smaller. In contrast, the Dice coefficient calculates twice the intersection divided by the sum of the sizes of both sets which emphasises true positives. Using both provides a more robust evaluation, enhancing the detection and deterrence of false positives.^{52,53}

2.3 | Mathematical formulation of EVEPR and choice in loss function

Mathematically, the EVEPR step in Figure 2B can be represented below.

$$I_{\text{PR}} = \mathcal{F}(I_{\text{dEEC}}; \theta). \quad (3)$$

In Equation (3), I_{PR} and I_{dEEC} represent the PR and denoised EEC images, respectively. The CNN is trained to learn the spatial mapping, \mathcal{F} , from I_{dEEC} to I_{PR} with θ representing the parameters of the CNN. To train this CNN, a loss function, \mathcal{L} , is minimised. The loss function represents the predicted image, \hat{I} , and the target image, I_{PR} , as follows.

$$\hat{I} = \mathcal{F}(I_{\text{dEEC}}; \arg \min \mathcal{L}(\theta)). \quad (4)$$

Three loss functions were considered for CNN training. Mean absolute error (L1) normalised cross correlation (NCC) and structural similarity index measure (SSIM). L1 calculates the absolute difference between target values and predictions which can be less sensitive to outliers. The NCC loss function is well suited for tasks where the alignment of the predicted and target images is critical. NCC aims to maximise the correlation between two images. The SSIM loss function is designed to preserve the visual quality of images by considering changes in texture, contrast, and luminance. SSIM maintains structural information.^{54–57} The results of all three loss functions and their combinations were observed. The L1, NCC, and SSIM loss functions that were tested in the training script are shown below.

$$L_1(x, y) = |x - y|, \quad (5)$$

$$\mathcal{L}(\theta) = \frac{1}{N} \sum_{i=1}^N |\mathcal{F}(I_{\text{dEEC},i}; \theta) - I_{\text{PR},i}|. \quad (6)$$

In Equation (5), x represents the input values, y represents the target values. In Equation (6), the sum of the absolute errors between images x and y are calculated over N , where N is the total number of data points (i.e., slices in the µCT stack) being processed.⁵⁸

$$\text{NCC}(x, y) = \frac{(x - \mu_x)(y - \mu_y)}{\sigma_x \sigma_y}, \quad (7)$$

$$\mathcal{L}(\theta) = \frac{1}{N} \sum_{i=1}^N (1 - \text{NCC}(\mathcal{F}(I_{\text{dEEC},i}; \theta), I_{\text{PR},i})). \quad (8)$$

In Equation (7), x and y are the input and target normalised from [0,1]. μ_x and μ_y are the mean and σ_x and σ_y are the standard deviations of the signals from x and

y . In Equation (8), the NCC loss is calculated as $1 - \text{NCC}(x, y)$.⁵⁶

$$\text{SSIM}(x, y) = \frac{(2\mu_x \mu_y + c_1)(2\sigma_{xy} + c_2)}{(\mu_x^2 + \mu_y^2 + c_1)(\sigma_x^2 + \sigma_y^2 + c_2)}, \quad (9)$$

$$\mathcal{L}(\theta) = \frac{1}{N} \sum_{i=1}^N (1 - \text{SSIM}(\mathcal{F}(I_{\text{dEEC},i}; \theta), I_{\text{PR},i})). \quad (10)$$

In Equation (9), x and y are the input and target; μ_x and μ_y are the average intensities; σ_x^2 and σ_y^2 are the variances; σ_{xy} is the covariance; c_1 and c_2 are the variables to stabilise the division of weak denominator and are given by $c_1 = (k_1 l)^2$ and $c_2 = (k_2 l)^2$, respectively; k_1 and k_2 were chosen as 0.01 and 0.03, respectively, as in the original article⁴⁶ and l is the dynamic range of the pixel values.⁵⁹ In Equation (10), the SSIM loss function is calculated as $1 - \text{SSIM}(x, y)$.⁶⁰

2.4 | Model architecture and training

CNN training and prediction used U-Net implemented through TensorFlow and Keras. U-Net has consistently shown to be capable in predicting artefact-free images by learning artefact corrupted input and target pairs without a priori references.^{15,13} Furthermore, U-Net was found to have performed better than similarly capable architectures i.e., MSD-Net and DD-Net.³⁰ A convolutional block consisted of two convolutional layers with ReLU activation and ‘same’ padding, used throughout the model. The U-Net model comprised four layers: (1) a downsampling path with convolutional blocks and max-pooling layers, (2) a bottleneck connecting the two paths, (3) an upsampling path followed by convolutional blocks, and (4) a final convolutional layer that produced the output. The model was configured with an input depth of three because µCT images are read and stored as three-dimensional raster.

A minibatch data generator which used prefetching for enhanced efficiency was used. The U-Net model was optimised using the Adam optimiser with a learning rate set to 10^{-4} , to ensure a balance between speed and stability during training, and default TensorFlow parameters of $\beta_1 = 0.9$, $\beta_2 = 0.999$, and $\epsilon = 10^{-7}$. The training loop was iterated over a user-specified number of epochs and each epoch included data normalisation based on the training µCT image bit depth. The generator loss was formed as the weighted sum of L1, MSE, NCC, and SSIM as specified by the user for training, the different combinations were investigated and shown in Section 3.5. The generator was updated once per epoch based on the specified number of iterations for training the generator. Periodically at a user-specified interval, the model prediction will be

saved to check on the progress. The images were cropped into patches of size 64×64 pixels, and training was performed in minibatches of 32. The model hyperparameters and architecture features were chosen to balance the speed and stability for training on a system running an Intel Xeon Silver 4210R processor and an NVIDIA A5000 graphics card with 128 GB of RAM. Typical data type and size is a tiff stack of 400 images, each image being 1024×1024 pixels. This could be 420 MB to 1.6 GB for each dataset depending on the chosen bit depth of the data. Training for 3000 epochs requires approximately 30 min.

2.5 | Preparation of hydrogel constructs for *in vitro* and *ex vivo* imaging

Hydrogel constructs made from biocompatible materials (i.e., alginate and gelatine) are used in tissue engineering and regenerative medicine to support cell growth and facilitate tissue regeneration.^{61–63} Hydrogel constructs have low density and PBI- μ CT shows unique advantages for hydrogel visualisation and characterisation.⁶⁴ The hydrogel constructs for *in vitro* imaging used in this study were prepared by following the procedure developed in our previously published studies.^{42,43} For studying the efficacy of hydrogel constructs in nerve tissue engineering, it is necessary to develop non-destructive imaging and characterisation methods.⁴² In this study, an *ex vivo* sample was created by implanting a hydrogel construct into an excised hindlimb of a euthanised animal near the site of the sciatic nerve. The procedure was performed with the approval of the University of Saskatchewan Committee on Animal Care and Supply.

3 | RESULTS

3.1 | Image processing results of low-density hydrogel constructs using EEC, PR, and EVEPR

This study presents EVEPR as an image processing method that resolves the issues present in PR and EEC images of low-density hydrogel constructs as shown in Figure 3. Looking at Figure 3A-1 and A-2 is a comparison between the unprocessed noisy EEC image and the denoised EEC image. The noisy EEC image exhibits excessive noise which prevents any meaningful analysis. Although sophisticated denoising can be used, the denoised EEC image exhibits bright-dark bands characteristic of X-ray phase shift do not correctly represent a material by a consistent grey value. Figure 3B-1 and B-2 is a comparison between the denoised EEC image and PR image. PR offers bet-

ter contrast between the hydrogel and the surrounding water, but variations in X-ray phase shift in materials can lead to spots with extremely bright phase contrast that obscures image features that were visible in the denoised EEC image. Furthermore, PR suffers from inconsistency in grey value as seen in water inside and outside of the hydrogel even though it is water all the same. Figure 3C-1 and C-2 is a comparison between the PR image and the proposed EVEPR image from this study. The EVEPR image is a CNN prediction trained on PR and denoised EEC image features which resulted in excellent contrast between the hydrogel construct and surroundings and improved consistency in material grey value. These qualities lead to more accurate segmentation, as shown in the comparison between Figure 3D-1 and D-2, which are simply grey value thresholds. The Dice scores of Figure 3D-1 and D-2 were 0.90 and 0.98, respectively, compared to a manual segmentation.

3.2 | Quantitative measures of EVEPR enhancement in SNR and CNR

The boundary definition of EEC and the quantitative area contrast of PR are complementary and when used to train a CNN, produced the EVEPR image result which overcome the challenges posed by each method alone. EVEPR strives for more accurate quantitative analysis shown in Figure 4, which presents a detailed comparison across six different image processing techniques applied towards PBI- μ CT of hydrogel constructs. Figure 4A-1–F-1 shows the same hydrogel sample processed as EVEPR, PR using TIE algorithm, PR using contrast transfer function (CTF) algorithm, PR using quadratic phase (QP) algorithm, denoised EEC, and noisy EEC images along with their respective SNR and CNR values as quantitative measures. The capability to distinguish the interior regions of the hydrogel material as well as the overall shape allowed for more precise binary segmentation through simple thresholding shown in Figure 4A-2–F-2. The Dice and Jaccard values were compared to a manually segmented ground truth. Only the EVEPR segmentation result achieved both Dice and Jaccard values above 0.9.

The summary of SNR and CNR for 84 hydrogel constructs samples are tabulated in Table 1 for six image processing methods used in this study with EVEPR demonstrating the highest image quality, specifically the SNR and CNR. The EEC results were excluded from analysis as it was already clear that they would be the worst performing. A Wilcoxon signed-rank test was conducted on EVEPR and TIE because TIE served as the input data which EVEPR enhanced and thus the two are not independent. For 84 observations for which all observations were improvements in SNR and CNR, the *p*-value was extremely

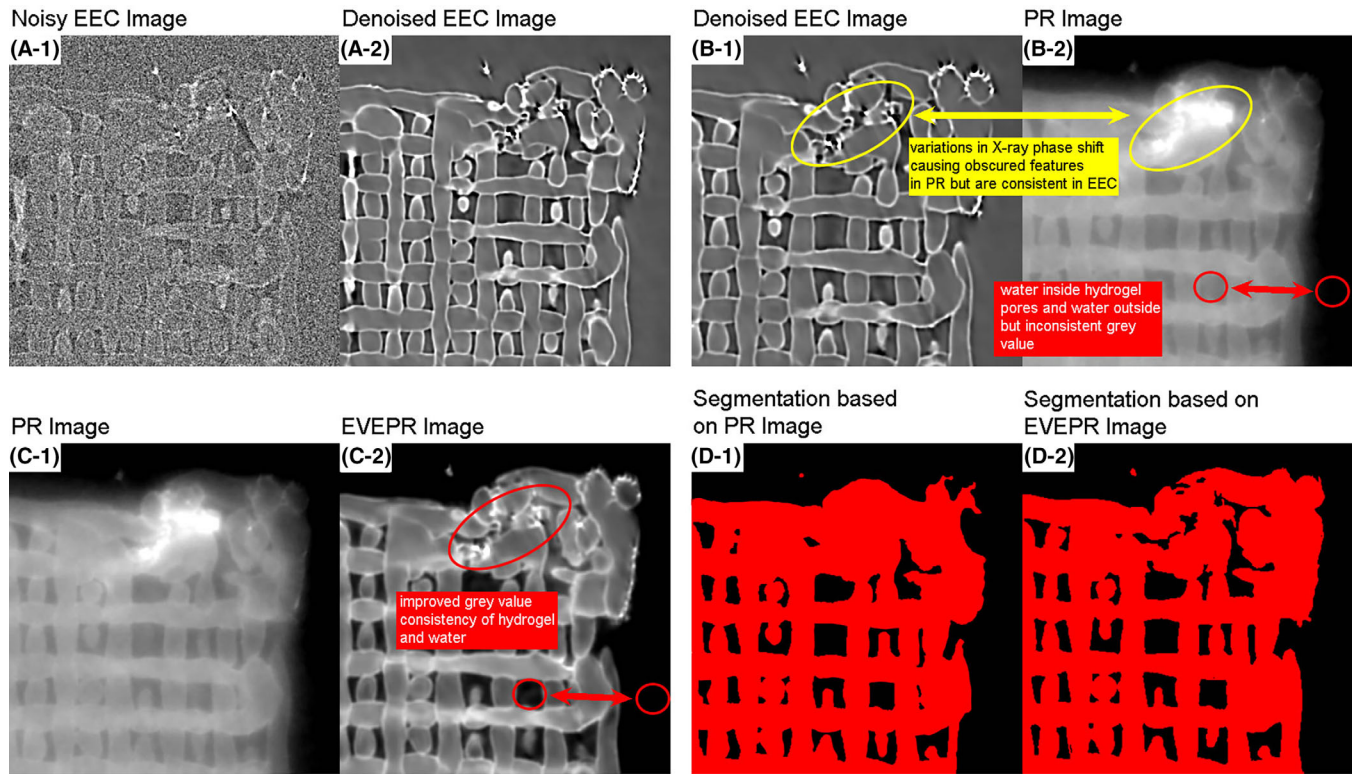


FIGURE 3 Different image processing results of low-density hydrogel construct through. (A-1), (A-2) Compare noisy and denoised EEC images. (B-1), (B-2) Compare denoised EEC and PR images. (C-1), (C-2) Compare the PR and EVEPR images. (D-1), (D-2) Show that the EVEPR image can lead to more accurate segmentation. The issues of obscured features and grey value inconsistencies are circled and labelled.

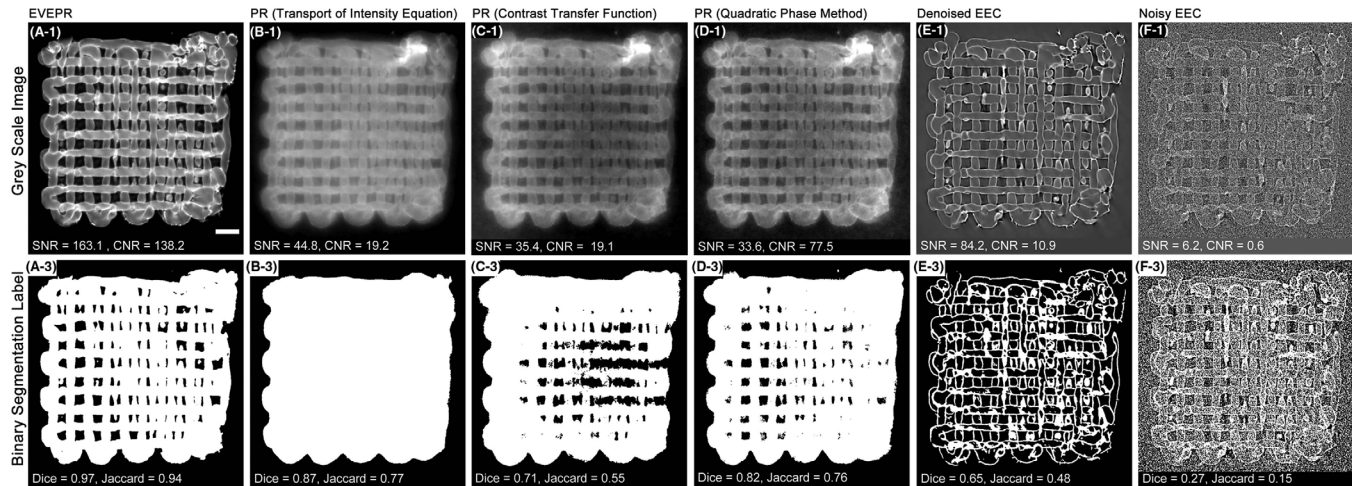


FIGURE 4 Comparison of binary segmentation results using different image processing methods of low-density hydrogel constructs: (A) EVEPR, (B) PR using TIE, (C) PR using CTF, (D) PR using QP, (E) denoised EEC, and (F) noisy EEC. The scale bar in (A-1) represents 1 mm.

TABLE 1 Summary of the SNR and CNR measures for six image processing results for 84 observations.

Measure	EVEPR	PR (TIE)	PR (CTF)	PR (QP)	Denoised EEC	Noisy EEC
SNR	148.5 ± 32.1	109.0 ± 44.7	93.9 ± 37.5	90.7 ± 28.6	81.2 ± 21.7	3.8 ± 1.0
CNR	80.7 ± 21.6	23.5 ± 5.9	21.5 ± 4.8	29.7 ± 11.8	11.2 ± 4.2	1.3 ± 0.5

TABLE 2 Calculating the statistical significance of quantitative measures significance with 99.9% confidence.

Group 1	Group 2	Post hoc Tukey's HSD for SNR			Post hoc Tukey's HSD for CNR		
		Mean difference	q-value	Significant	Mean difference	q-value	Significant
EVEPR	CTF	56.1	0.001	Yes	58.7	0.001	Yes
EVEPR	QP	-58.5	0.001	Yes	-50.3	0.001	Yes
CTF	QP	-2.4	0.9	No	8.3	0.004	Yes

small at 8.55×10^{-16} . This statistical test validates that the EVEPR results were not random and worked as expected every time.

Among the PR results in Figure 4B–D, the grey value contrast within the hydrogel material was lower compared to the contrast between the hydrogel and its surroundings. This was particularly noticeable in the TIE result and attempting to threshold the hydrogel from the surroundings could not identify the pores of the hydrogel. The CTF and QP results showed better grey value contrast within the hydrogel also contained noticeable shadows and grey value inconsistencies lead to inaccuracies in the rough segmentation result. These inaccuracies need to be manually corrected as opposed to the straightforward use of a threshold to obtain an accurate but rough segmentation which is possible using EVEPR.

One-way ANOVA with post hoc tests were performed on EVEPR, CTF, and QP as these were independent groups. The TIE and EVEPR images were not considered as TIE images were used in training to obtain EVEPR result. It was found that the *f*-value was 26.7 for SNR and 135.4 for CNR. These exceed the critical *f*-value for a 99.9% confidence for 84 observations and 3 groups which suggests that these image processing techniques substantially affect the quality of the image enhancement, with some techniques outperforming others in terms of SNR and CNR. To find out which, a post hoc Tukey's HSD statistic for each group pair was performed and shown in Table 2. This analysis confirms strong significant performance disparities in both SNR and CNR when comparing the EVEPR technique against CTF and QP. The EVEPR result has demonstrated consistent superior image enhancement capabilities that are statistically significant. Meanwhile, the difference in SNR between CTF and QP was not statistically significant with QP CNR slightly higher than CTF CNR.

To further support that EVEPR demonstrated superior SNR and CNR, a grey value profile across a hydrogel material shown in Figure 5 and presents a comparative analysis for each of the image processing methods investigated. The grey value profile for each image showed variation in contrast and visible detail across the hydrogel material. Notably, profile across the EVEPR image exhibited the highest contrast, clearly delineating the hydrogel strands, while also showing consistent grey value across

the hydrogel and water. Subsequently, Figure 5B–1–D–1 displays PR image results which used TIE, CTF, and QP with varying capability for quantitative area contrast over the hydrogel material. The grey value profile across the TIE and CTF images show a distinct trajectory with the grey value of each hydrogel strand whereas the EVEPR profile showed a consistent grey value. In addition, the grey value profile across the QP image showed greatest noise among the PR results. In Figure 5E–1, the denoised EEC image shows extremely well-defined boundaries but not the crucial area contrast required for segmentation. Lastly, the unprocessed EEC image in Figure 5F–1 shows noise significantly masks the structural details.

3.3 | Choice in loss function

The performances of L1, NCC, and SSIM as loss functions were assessed in the denoising step. The effectiveness of each loss function was quantified by measuring the SNR and CNR of the denoised prediction as well as the ground truth (GT). Figure 6 shows the three chosen loss functions as well as their combinations. This demonstrated an increase in SNR with the equally weighted NCC and SSIM loss performing the best. The CNR did not show as significant of an improvement from the GT, likely because the low-density hydrogel shared a grey value profile to the water in which it was submerged. The SNR and CNR evaluations of the predicted result when the training used combinations of loss functions. The combined loss function was an equally weighted sum of L1, NCC, and SSIM. It was found that the combination of NCC and SSIM performed the best with the highest SNR and CNR. Any combination with L1 loss produced a similar result to L1 loss alone. The predicted result from SSIM loss suffered quite heavily from minor variations between input and target data.

In Figure 7, the CNN predicted results are shown. Individual loss functions L1, NCC, and SSIM each exhibited improvements to SNR with SSIM having the greatest increase in CNR as well. The combined losses lead to some balanced improvement, but the exact configuration of these combinations can have a substantial impact, as seen with the L1-NCC-SSIM combination, which does not

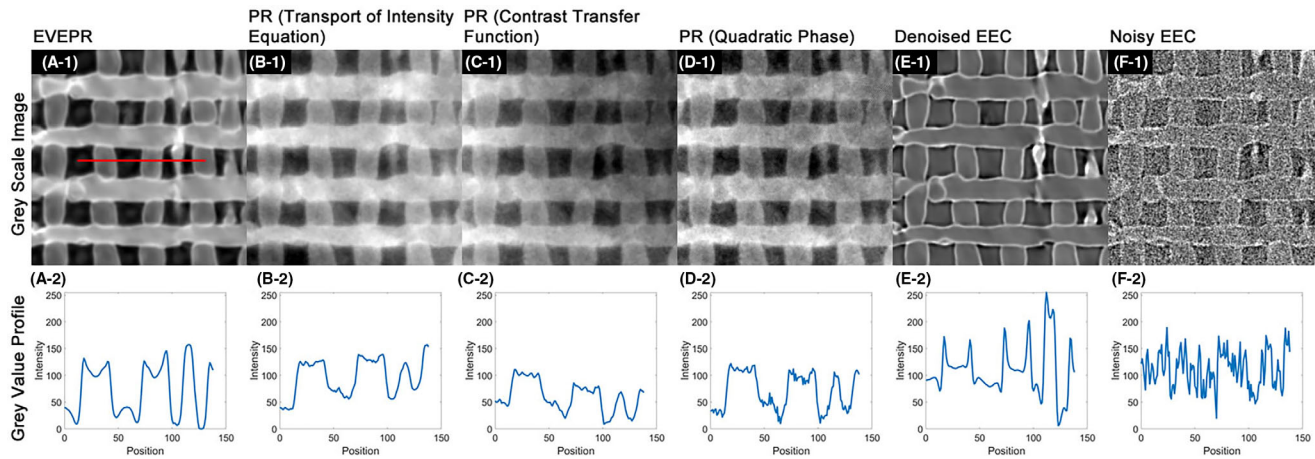


FIGURE 5 The grey value profile across the hydrogel construct strands using different image processing methods.

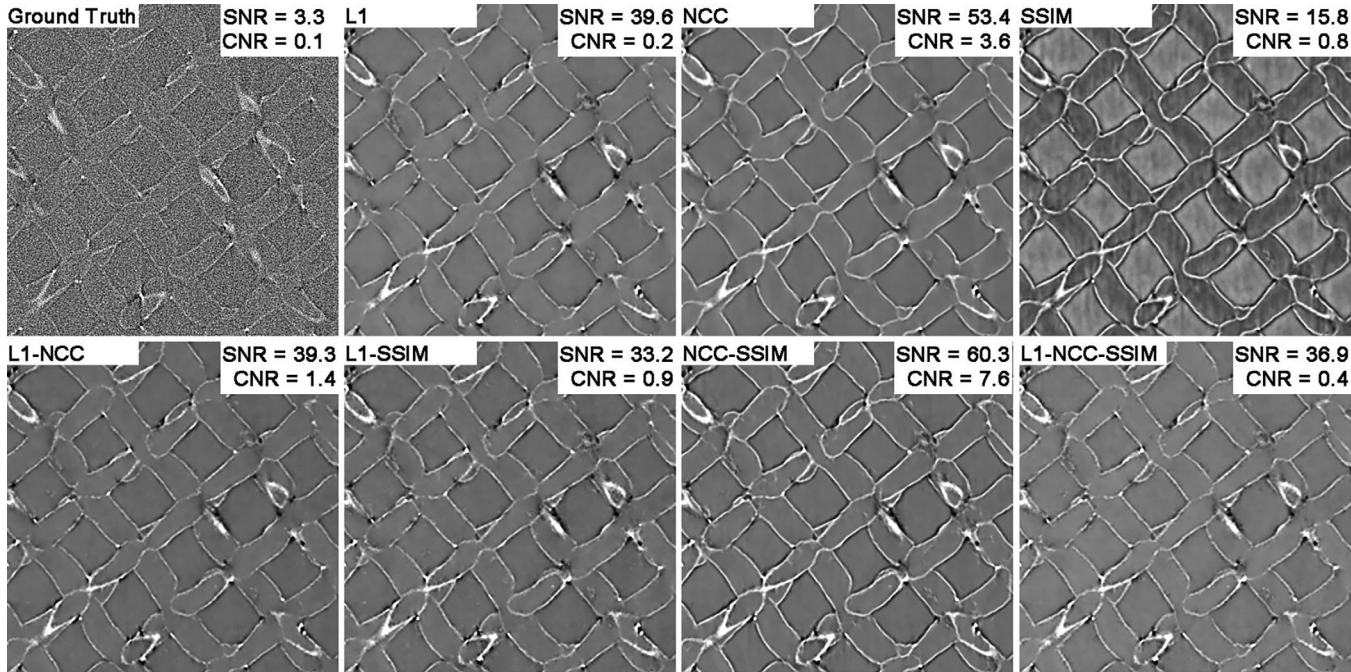


FIGURE 6 Comparison of SNR and CNR for noisy ground truth (GT) as well as the denoised result using L1, NCC, and SSIM loss functions. Also shown are the combinations of loss functions, with each loss weighted equally and the SNR and CNR for each result.

perform as well as the others, possibly due to conflicting gradients or error signals in the loss function landscape. Overall, SSIM alone outperformed the downsides of any combination of losses when equally weighted with the increase in SNR and CNR.

To visualise the two rounds of training with different loss functions, the normalised loss values across several thousand epochs was plotted in Figure 8. Only the individual loss plots were shown with the combination losses exhibiting similar behaviours to their constituent losses. The loss trajectories shown provide an understanding of

the efficiency in training. For denoising, both NCC and SSIM losses performed better than L1. Figure 8A showed the L1 reached zero too quickly which could indicate premature convergence. NCC and SSIM losses exhibited more volatility but displayed a gradual convergence, indicating the model was learning the spatial information. In Figure 8B, the same loss functions were used to train on learning EEC and PR spatial features. For this purpose, the NCC loss exhibited the most volatility and L1 exhibited sudden spikes, neither of which were seen compared to SSIM. Consequently, any weighted combination with

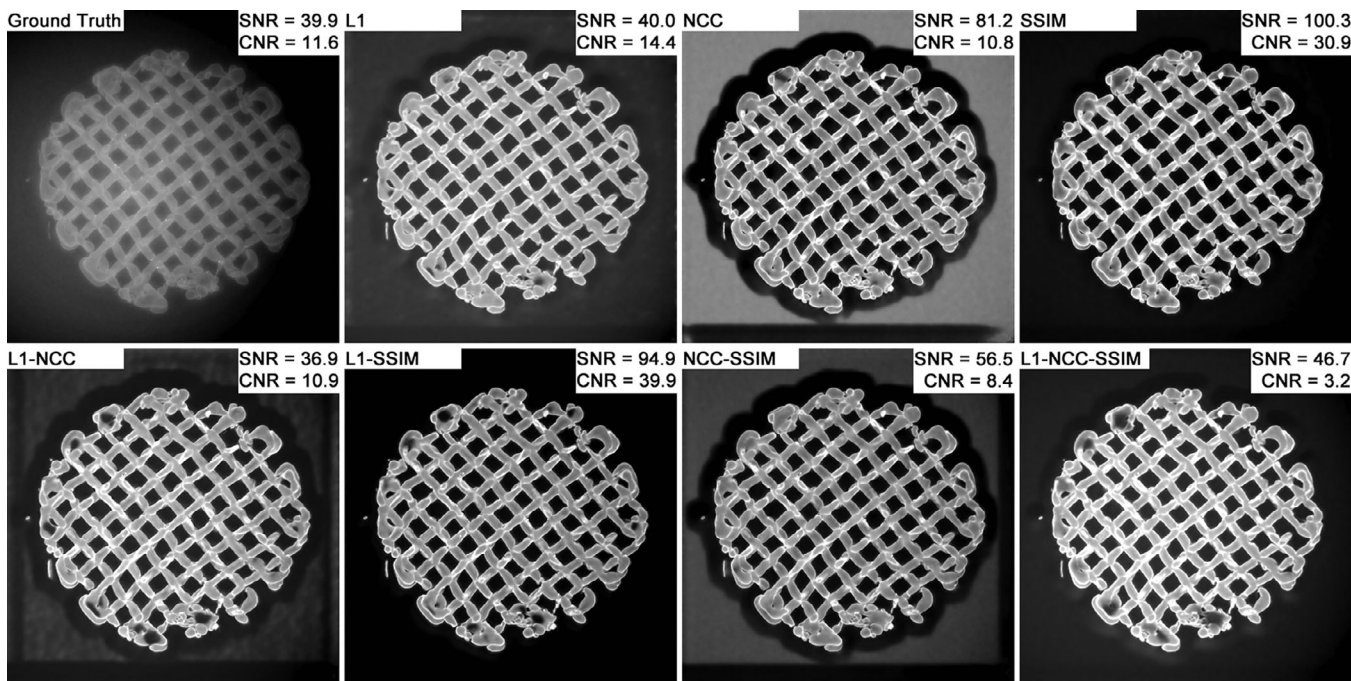


FIGURE 7 Comparison of SNR and CNR for PR ground truth (GT) as well as the EVEPR result using L1, NCC, and SSIM as loss functions. Also shown are the combinations of loss functions, with each loss weighted equally and the SNR and CNR for each result.

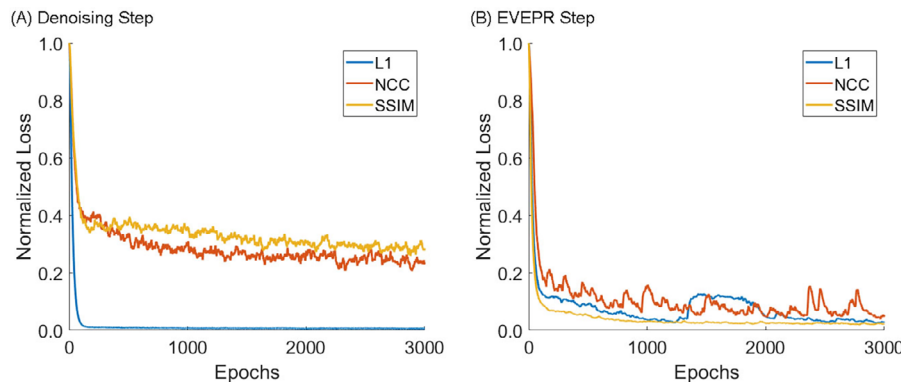


FIGURE 8 Plotting the normalised loss values plotted over 3000 training epochs for models trained with L1, NCC, and SSIM loss functions for (A) denoising and (B) EVEPR.

NCC or L1 performed worse than SSIM alone, which is consistent with the results in Figure 7.

3.4 | Application of EVEPR for data-driven model-based segmentation

As was shown in Section 3.2, EVEPR can improve the SNR and CNR through deep learning on the strengths of PR and EEC images. This enhanced CNR especially, facilitated more efficient segmentation results. Illustrated in Figure 9 are the full 3D segmentation results using a random-walk interpolation with EVEPR and PR images as the underly-

ing image data. It was found that working with EVEPR required fewer presegmented slices to achieve Dice and Jaccard values greater than 0.9. Furthermore, the time required to obtain one presegmented EVEPR slice was 13 ± 2 min as opposed to 28 ± 7 min when segmenting the PR image data.

The improved efficiency in segmentation allowed for a database of 84 fully segmented hydrogel construct labels to be compiled. The fully segmented labels were paired with images for conventional data-driven deep learning training for model-predicted automatic segmentation. Of the 84 hydrogel constructs observed, 83 were used to train data-driven segmentation models and one was kept aside to test

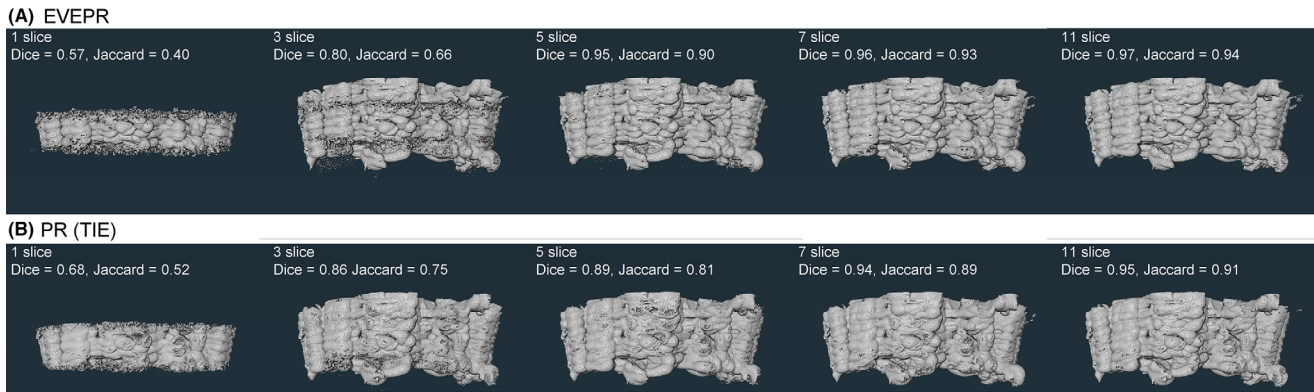


FIGURE 9 The segmentation efficiency for different image processing methods: (A) EVEPR and (B) PR using TIE.

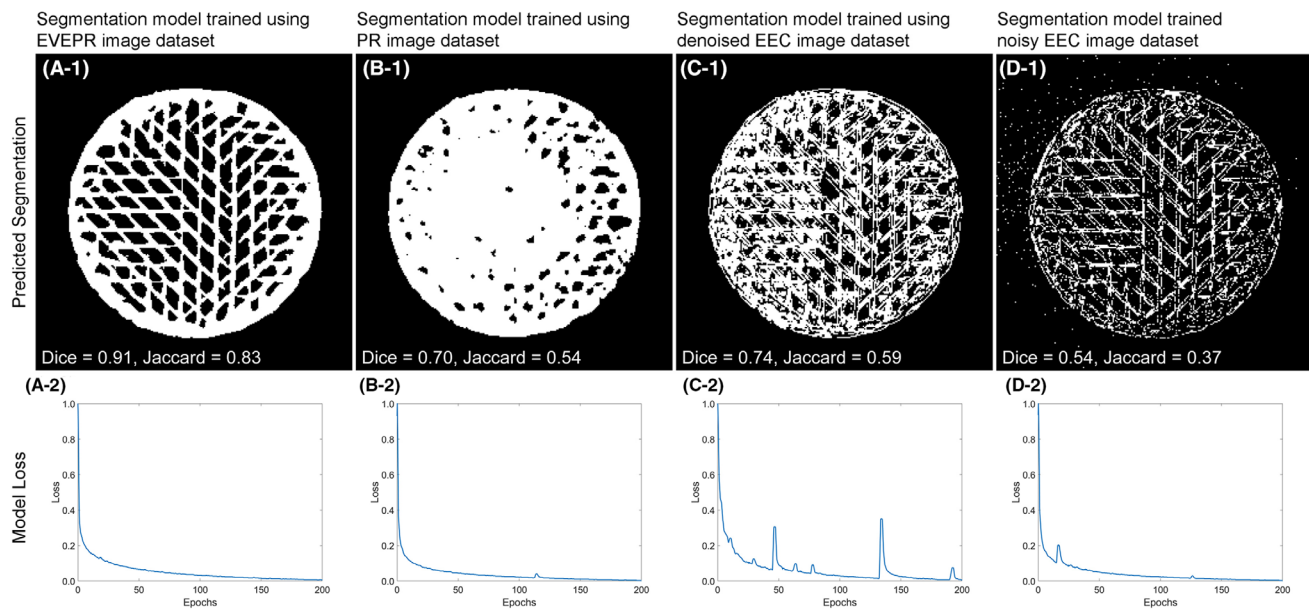


FIGURE 10 Comparison of segmentation performance by deep learning models on PBI- μ CT images processed by EVEPR, PR, denoised EEC, and noisy EEC. (A-1)–(D-1) The model predicted segmentation of the test image with Dice and Jaccard values evaluated. (A-2)–(D-2) The loss over 200 epochs is shown.

the models to prevent overfitting, augmentation strategies of rotating, flipping, stretching, and intensity normalisation were applied to the data at random. To train a model, the label and image pairs were partitioned into a conventional 80/20 split for training and validation.⁶⁵ Four models were trained using differently processed images: EVEPR, PR using TIE, denoised EEC, and noisy EEC. The result from each of the four models on the test hydrogel construct μ CT stack that was kept aside is shown in Figure 10.

The model predicted segmentation results are shown in Figure 10A-1–D-1. The Dice and Jaccard values were used to quantify segmentation accuracy for which the model trained on EVEPR images showing the greatest accuracy. Figure 10A-2–D-2 shows the loss over training epochs, offering insight into the learning efficiency and

convergence behaviour of each model. The EVEPR strategy enhanced SNR and CNR, leading to the most accurate segmentation results, while the other methods display varying degrees of success, with the unprocessed images resulting in the poorest performance due to low SNR and CNR. The model-predicted results show the robustness of the EVEPR strategy in the successful segmentation of a test image despite the modest size of the database.

3.5 | Application in segmenting ex vivo results

EVEPR was used for analysing ex vivo μ CT images of a hydrogel construct implanted in a Sprague–Dawley rat's

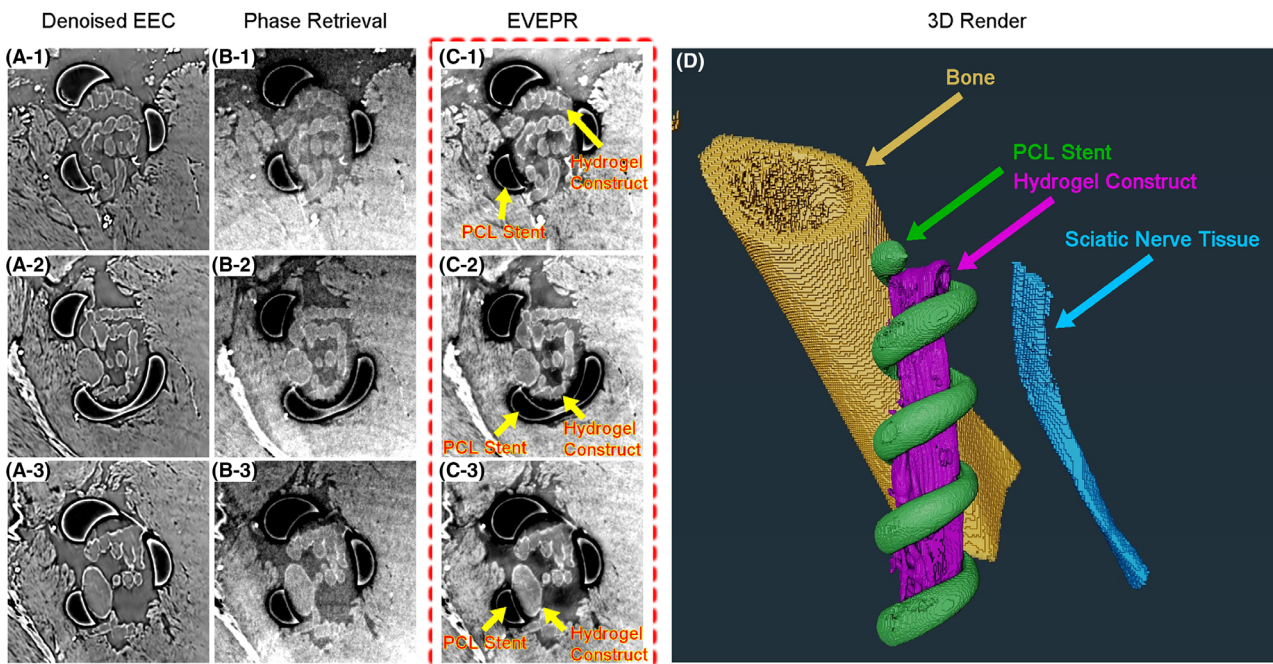


FIGURE 11 Ex vivo images of hydrogel construct implant in a Sprague–Dawley rat hindlimb processed using (A) denoised EEC, (B) phase retrieval, and (C) EVEPR. Arrows pointing to the PCL stent and hydrogel construct. Outside of the stent is the surrounding tissue and inside the is just hydrogel and body fluid. (D) 3D render of not only the PCL stent and hydrogel construct, but also the sciatic nerve and femur bone.

excised hindlimb. The hydrogel construct, designed for sciatic nerve injury repair, was inserted within a polycaprolactone (PCL) stent for mechanical protection and implanted at the site of sciatic nerve. The denoised EEC, PR, and EVEPR images of the hydrogel construct and stent at different slices are shown in Figure 11A–C. A detailed 3D render that shows a section of the femur bone, PCL stent, hydrogel construct, and sciatic nerve tissue in Figure 11D.

The EVEPR strategy was most effective for CT images consisting of two distinct materials where one material fully encompasses the other. This was grounded in the physics of the TIE–Hom algorithm used for phase retrieval. However, the ex vivo data will undoubtedly contain a mix of materials (e.g., muscle, fat, bone, etc.), posing a challenge for a straightforward application of EVEPR. To address this, ex vivo images were cropped to where it contained fewer image details, which could provide more consistent supervisory signals in the CNN training procedure. The hydrogel construct exhibited a similar grey value to the surrounding muscle tissue and from a deep learning perspective, these could be understood by the training network as one material as the grey value inhabit the same part of the grey value histogram of the overall images. Within the PCL stent, there was only scaffold and body fluid. By cropping the ex vivo images, this reduced the complexity of the images aligning with the optimal conditions for EVEPR. The SNR of the denoised EEC, phase

retrieved, and EVEPR images were 5.92 ± 1.22 , 18.87 ± 1.83 , and 21.10 ± 2.65 , respectively. The CNR of the denoised EEC, phase retrieved, and EVEPR images were 2.33 ± 0.22 , 2.67 ± 0.70 , and 4.19 ± 1.03 , respectively. The improved grey value consistency in the EVEPR ex vivo results allowed for effective segmentation and 3D modelling shown in Figure 11D.

4 | DISCUSSION

The development of the EVEPR strategy shows an advancement in PBI- μ CT image processing and demonstrated through its enhancement of phase contrast image quality. This paper has demonstrated that training a deep CNN on complementary spatial features present in denoised EEC and PR images can significantly improve the visualisation of low-density materials, notably demonstrated on hydrogel constructs, which are challenging to image using conventional methods. The EVEPR approach not only significantly enhances both SNR and CNR but also improved consistency in grey value across materials. Statistically, the SNR and CNR as metrics to measure image quality improvements has shown that EVEPR consistently outperformed conventional PR methods. These metrics are critical as they directly relate to the practical utility of the processed images in segmenting hydrogel constructs *in vitro* and *ex vivo*.

The ex vivo results presented the feasibility of applying EVEPR for biomedical research applications. The successful segmentation and visualisation of the hydrogel construct, PCL stent, sciatic nerve, and femur bone in the rat hindlimb demonstrate the potential of EVEPR in analysing multi-material samples as part of segmentation strategy. PBI- μ CT is widely regarded as the most popular phase contrast imaging because it is the simplest to put into practice. By enhancing the contrast of PR images, the EVEPR strategy can extend its applications to in vivo imaging as low-dose image acquisition and image processing strategies are developed.^{30,66,67}

The improved image quality in EVEPR allowed for efficient and accurate segmentation. When applied to different scans of hydrogel constructs, the image processing and CNN training hyperparameters were not expected to change for PBI scans of different hydrogel samples because the X-ray interaction with the hydrogel material was not expected to be different. This effectively streamlined the segmentation task for hydrogels once the parameters had been optimised and minimised the time in dataset batches and time devoted to specific adjustments. Starting from a dataset-to-dataset basis, a sufficient database could be generated for data-driven model-predicted segmentation as demonstrated with hydrogel constructs in this study.

The contribution of this work is a deep learning training strategy for learning the spatial information from paired denoised EEC and PR images as a valuable tool for niche research areas. The target research areas which EVEPR could be applicable are low-density material research using PBI- μ CT, that is, studying the internal structures of soft metals,⁶⁸ foams,⁶⁹ aerogels,⁷⁰ biomaterials,⁷¹ and pharmaceutical formulations.^{72–74} The key to EVEPR was realising that phase contrast imaging typically displays images which contrast is from X-ray phase shift with X-ray absorption together. However, low-density materials are too weakly absorbing to be visible with absorption-contrast, such that the denoised EEC image reveals only the characteristic light-dark fringe pairs running along edges and boundaries from the phase shift. The denoised EEC image without absorption-contrast was the spatial information that would be lost from over-smoothing in the PR image and thus, a deep learning CNN could be trained to learn the complementary spatial features. The predicted EVEPR image was not known, thus, there was no a priori reference as part of the CNN training.

5 | CONCLUSIONS

EVEPR is a post image processing strategy that uses paired denoised EEC and PR images trained through a deep CNN to enhance the image features without rely-

ing on a priori references. By training on important high-frequency details and minimising noise, EVEPR significantly improved the SNR and CNR as well improved the consistency in grey value contrast. This enabled accurate segmentation and detailed characterisation of low-density materials. Furthermore, the efficiency in generating a database of segmentation labels and potential for model-predicted segmentation presents the applicability of EVEPR in segmentation of low-density material studies, such as hydrogel construct in vitro or ex vivo studies.

ACKNOWLEDGEMENTS

This work was supported by the University of Saskatchewan Graduate Scholarship, NSERC INSPIRE Graduate Fellowship, and the NSERC Discovery grant (NSERC, No. RGPIN 06007-2019 and No. RGPIN 06396-2019). Part or all of the research described in this paper was performed at the Canadian Light Source, a national research facility of the University of Saskatchewan, which is supported by the Canada Foundation for Innovation (CFI), the Natural Sciences and Engineering Research Council (NSERC), the National Research Council (NRC), the Canadian Institutes of Health Research (CIHR), the Government of Saskatchewan, and the University of Saskatchewan.

DATA AVAILABILITY STATEMENT

Training script is available at <https://github.com/xfding57/EdgeView-Segmentation>. The datasets used and/or analysed for this manuscript are available from the corresponding author on reasonable request.

ORCID

- Xiao Fan Ding  <https://orcid.org/0000-0002-2137-6002>
- Xiaoman Duan  <https://orcid.org/0000-0003-1221-1609>
- Naitao Li  <https://orcid.org/0000-0002-3679-0505>
- Zahra Khoz  <https://orcid.org/0009-0009-5695-7016>
- Fang-Xiang Wu  <https://orcid.org/0000-0002-4593-9332>
- Xiongbiao Chen  <https://orcid.org/0000-0002-4716-549X>
- Ning Zhu  <https://orcid.org/0000-0002-2633-9956>

REFERENCES

1. Gureyev, T. E., Mayo, S. C., Myers, D. E., Nesterets, Y., Paganin, D. M., Pogany, A., Stevenson, A. W., & Wilkins, S. W. (2009). Refracting Röntgen's rays: Propagation-based X-ray phase contrast for biomedical imaging. *Journal of Applied Physics*, 105(10), 102005. <https://doi.org/10.1063/1.3115402>
2. Zhou, S. A., & Brahme, A. (2008). Development of phase-contrast X-ray imaging techniques and potential medical applications. *Physica Medica*, 24(3), 129–148. <https://doi.org/10.1016/j.ejmp.2008.05.006>
3. Yoneyama, A., Yamada, S., & Take, T. (2011). Fine biomedical imaging using X-ray phase-sensitive technique. In

- D. G. Gaetano and M. Alistair (Eds.), *Advanced Biomedical Engineering*. InTech. <https://doi.org/10.5772/20456>
4. Mayo, S., & Endrizzi, M. (2019). X-ray phase contrast methods. In N. Ida and M. Norbert (Eds.), *Handbook of Advanced Nondestructive Evaluation*. Springer International Publishing. https://doi.org/10.1007/978-3-319-26553-7_54
5. Lynn, N. D., Sourav, A. I., & Santoso, A. J. (2021). Implementation of real-time edge detection using Canny and Sobel Algorithms. *IOP Conference Series: Materials Science and Engineering*, 1096(1), 012079. <https://doi.org/10.1088/1757-899x/1096/1/012079>
6. Razali, M. R. M., Ahmad, N. S., Hassan, R., Zaki, Z. M., & Ismail, W. (2015). Sobel and Canny edges segmentations for the dental age assessment. In *Proceedings of the 2014 International Conference on Computer Assisted System in Health, CASH 2014* (pp. 62–66). Institute of Electrical and Electronics Engineers Inc. <https://doi.org/10.1109/CASH.2014.10>
7. Nugent, K. A., Gureyev, T. E., Cookson, D. F., Paganin, D., & Barnea, Z. (1996). Quantitative phase imaging using hard X rays. *Physical Review Letter*, 77(14), 2961–2964. <https://doi.org/10.1103/PhysRevLett.77.2961>
8. Brombal, L. (2020). Effectiveness of X-ray phase-contrast tomography: Effects of pixel size and magnification on image noise. *Journal of Instrumentation*, 15, C01005. <https://doi.org/10.1088/1748-0221/15/01/C01005>
9. Diwakar, M., & Kumar, M. (2018). A review on CT image noise and its denoising. *Biomedical Signal Processing and Control*, 42, 73–88. <https://doi.org/10.1016/j.bspc.2018.01.010>
10. Buades, A., Coll, B., & Morel, J. M. (2011). Non-local means denoising. *Image Processing On Line*, 1, 208–212. https://doi.org/10.5201/ipol.2011.bcm_nlm
11. Buades, A., Coll, B., & Morel, J. M. (2005). A review of image denoising algorithms, with a new one. *Multiscale Modeling and Simulation*, 4(2), 490–530. <https://doi.org/10.1137/040616024>
12. Flenner, S., Bruns, S., Longo, E., Parnell, A. J., Stockhausen, K. E., Müller, M., & Greving, I. (2022). Machine learning denoising of high-resolution X-ray nanotomography data. *Journal of Synchrotron Radiation*, 29, 230–238. <https://doi.org/10.1107/S1600577521011139>
13. Hendriksen, A. A., Pelt, D. M., & Batenburg, K. J. (2020). Noise2Inverse: Self-supervised deep convolutional denoising for tomography. *IEEE Transactions on Computational Imaging*, 6, 1320–1335. <https://doi.org/10.1109/TCI.2020.3019647>
14. Batson, J., & Royer, L. (2019). Noise2Self: Blind Denoising by Self-Supervision. Published online January 30, 2019. <http://arxiv.org/abs/1901.11365>
15. Lehtinen, J., Munkberg, J., Hasselgren, J., Laine, S., Karras, T., Aittala, M., & Aila, T. (2018). Noise2Noise: Learning image restoration without clean data. Published online March 12, 2018. <http://arxiv.org/abs/1803.04189>
16. Zanette, I., Bech, M., Pfeiffer, F., & Weitkamp, T. (2011). Interlaced phase stepping in phase-contrast X-ray tomography. *Applied Physics Letters*, 98(9), 094101. <https://doi.org/10.1063/1.3559849>
17. Mayo, S. C., Davis, T. J., Gureyev, T. E., Miller, P. R., Paganin, D., Pogany, A., Stevenson, A. W., & Wilkins, S. W. (2003). X-ray phase-contrast microscopy and microtomography. *Optics Express*, 11(19), 2289. <https://doi.org/10.1364/OE.11.002289>
18. Burvall, A., Lundström, U., Takman, P. A. C., Larsson, D. H., & Hertz, H. M. (2011). Phase retrieval in X-ray phase-contrast imaging suitable for tomography. *Optics Express*, 19(11), 10359. <https://doi.org/10.1364/OE.19.010359>
19. Bronnikov, A. V. (1999). Reconstruction formulas in phase-contrast tomography. *Optics Communications*, 171, 239–244. www.elsevier.com/locatordoptcom
20. Wu, X., & Liu, H. (2005). X-Ray cone-beam phase tomography formulas based on phase-attenuation duality. *Optics Express*, 13(16), 6000. <https://doi.org/10.1364/OPEX.13.006000>
21. Paganin, D., Mayo, S. C., Gureyev, T. E., Miller, P. R., & Wilkins, S. W. (2002). Simultaneous phase and amplitude extraction from a single defocused image of a homogeneous object. *Journal of Microscopy*, 206(1), 33–40. <https://doi.org/10.1046/j.1365-2818.2002.01010.x>
22. Beltran, M. A., Paganin, D. M., Uesugi, K., & Kitchen, M. J. (2010). 2D and 3D X-ray phase retrieval of multi-material objects using a single defocus distance. *Optics Express*, 18(7), 6423. <https://doi.org/10.1364/OE.18.006423>
23. Irvine, S., Mokso, R., Modregger, P., Wang, Z., Marone, F., & Stampanoni, M. (2014). Simple merging technique for improving resolution in qualitative single image phase contrast tomography. *Optics Express*, 22(22), 27257. <https://doi.org/10.1364/oe.22.027257>
24. Croton, L. C. P., Morgan, K. S., Paganin, D. M., Kerr, L. T., Wallace, M. J., Crossley, K. J., Miller, S. L., Yagi, N., Uesugi, K., Hooper, S. B., & Kitchen, M. J. (2018). In situ phase contrast X-ray brain CT. *Scientific Reports*, 8(1), 11412. <https://doi.org/10.1038/s41598-018-29841-5>
25. Ronneberger, O., Fischer, P., & Brox, T. (2015). U-Net: Convolutional networks for biomedical image segmentation. Published online May 18, 2015. <https://doi.org/10.48550/arXiv.1505.04597>
26. He, K., Gkioxari, G., Dollár, P., & Girshick, R. (2017). Mask R-CNN. Published online March 20, 2017. <http://arxiv.org/abs/1703.06870>
27. Chen, L. C., Zhu, Y., Papandreou, G., Schroff, F., & Adam, H. (2018). Encoder-decoder with atrous separable convolution for semantic image segmentation. Published online February 7, 2018. <http://arxiv.org/abs/1802.02611>
28. Tan, M., & Le, Q. V. (2019). EfficientNet: Rethinking model scaling for convolutional neural networks. Published online May 28, 2019. <http://arxiv.org/abs/1905.11946>
29. Isensee, F., Jaeger, P. F., Kohl, S. A. A., Petersen, J., & Maier-Hein, K. H. (2021). nnU-Net: A self-configuring method for deep learning-based biomedical image segmentation. *Nature Methods*, 18(2), 203–211. <https://doi.org/10.1038/s41592-020-01008-z>
30. Duan, X., Ding, X. F., Li, N., Wu, F. X., Chen, X., & Zhu, N. (2023). Sparse2Noise: Low-dose synchrotron X-ray tomography without high-quality reference data. *Computers in Biology and Medicine*, 165, 107473. <https://doi.org/10.1016/j.combiomed.2023.107473>
31. Wang, K., Song, L. i., Wang, C., Ren, Z., Zhao, G., Dou, J., Di, J., Barbastathis, G., Zhou, R., Zhao, J., & Lam, E. Y. (2024). On the use of deep learning for phase recovery. *Light: Science and Applications*, 13(1), 4. <https://doi.org/10.1038/s41377-023-01340-x>
32. Rivenson, Y., Zhang, Y., Günaydin, H., Teng, D., & Ozcan, A. (2017). Phase recovery and holographic image reconstruction using deep learning in neural networks. *Light: Science and Applications*, 6(1), 17001. <https://doi.org/10.1038/s41377-017-0001>

- Applications*, 7(2), 17141–17141. <https://doi.org/10.1038/lsa.2017.141>
33. Huang, L., Chen, H., Liu, T., & Ozcan, A. (2023). Self-supervised learning of hologram reconstruction using physics consistency. *Nature Machine Intelligence*, 5(8), 895–907. <https://doi.org/10.1038/s42256-023-00704-7>
34. Wu, X., Wu, Z., Shanmugavel, S. C., Yu, H. Z., & Zhu, Y. (2022). Physics-informed neural network for phase imaging based on transport of intensity equation. *Optics Express*, 30(24), 43398. <https://doi.org/10.1364/oe.462844>
35. Muralidhar, N., Islam, M. R., Marwah, M., Karpatne, A., & Ramakrishnan, N. (2018). Incorporating prior domain knowledge into deep neural networks. In *2018 IEEE International Conference on Big Data (Big Data)* (pp. 36–45). IEEE. <https://doi.org/10.1109/BigData.2018.8621955>
36. Li, F., Zhao, Y., Han, S., Ji, D., Li, Y., Zheng, M., Lv, W., Jian, J., Zhao, X., & Hu, C. (2022). Physics-informed deep neural network reconstruction framework for propagation-based x ray phase-contrast computed tomography with sparse-view projections. *Optics Letters*, 47(16), 4259. <https://doi.org/10.1364/OL.466306>
37. Zhang, Y., Andreas Noack, M., Vagovic, P., Fezzaa, K., Garcia-Moreno, F., Ritschel, T., & Villanueva-Perez, P. (2021). PhaseGAN: A deep-learning phase-retrieval approach for unpaired datasets. *Optics Express*, 29(13), 19593. <https://doi.org/10.1364/OE.423222>
38. Yao, Y., Chan, H., Sankaranarayanan, S., Balaprakash, P., Harder, R. J., & Cherukara, M. J. (2022). AutoPhaseNN: Unsupervised physics-aware deep learning of 3D nanoscale Bragg coherent diffraction imaging. *NPJ Computational Materials*, 8(1), 124. <https://doi.org/10.1038/s41524-022-00803-w>
39. Chen, X., Wang, H., Razi, A., Kozicki, M., & Mann, C. (2023). DH-GAN: A physics-driven untrained generative adversarial network for holographic imaging. *Optics Express*, 31(6), 10114. <https://doi.org/10.1364/OE.480894>
40. Wu, Y., Zhang, L., Guo, S., Zhang, L., Gao, F., Jia, M., & Zhou, Z. (2022). Enhanced phase retrieval via deep concatenation networks for in-line X-ray phase contrast imaging. *Physica Medica*, 95, 41–49. <https://doi.org/10.1016/j.ejmp.2021.12.017>
41. Gasilov, S., Webb, M. A., Panahifar, A., Zhu, N., Marinos, O., Bond, T., Cooper, D. M. L., & Chapman, D. (2024). Hard X-ray imaging and tomography at the biomedical imaging and therapy beamlines of Canadian light source. *Journal of Synchrotron Radiation*, 31(Pt 5), 1346–1357. <https://doi.org/10.1107/S1600577524005241>
42. Ning, L., Zhu, N., Smith, A. n., Rajaram, A., Hou, H., Srinivasan, S., Mohabatpour, F., He, L., McInnes, A., Serpooshan, V., Papagerakis, P., & Chen, X. (2021). noninvasive three-dimensional *in situ* and *in vivo* characterization of bioprinted hydrogel scaffolds using the X-ray propagation-based imaging technique. *ACS Applied Materials & Interfaces*, 13(22), 25611–25623. <https://doi.org/10.1021/acsami.1c02297>
43. Duan, X., Li, N., Cooper, D. M. L., Ding, X. F., Chen, X., & Zhu, N. (2023). Low-density tissue scaffold imaging by synchrotron radiation propagation-based imaging computed tomography with helical acquisition mode. *Journal of Synchrotron Radiation*, 30(Pt 2), 417–429. <https://doi.org/10.1107/S1600577523000772>
44. Faragó, T., Gasilov, S., Emslie, I., Zuber, M., Helfen, L., Vogelgesang, M., & Baumbach, T. (2022). Tofu: A fast, versatile and user-friendly image processing toolkit for computed tomography. *Journal of Synchrotron Radiation*, 29(3), 1–12. <https://doi.org/10.1107/S160057752200282X>
45. Münch, B., Trtik, P., Marone, F., & Stampanoni, M. (2009). Stripe and ring artifact removal with combined wavelet—Fourier filtering. *Optics Express*, 17(10), 8567. <https://doi.org/10.1364/OE.17.008567>
46. Yao, L., Zeng, D., Chen, G., Liao, Y., Li, S., Zhang, Y., Wang, Y., Tao, X. i., Niu, S., Lv, Q., Bian, Z., Ma, J., & Huang, J. (2019). Multi-energy computed tomography reconstruction using a nonlocal spectral similarity model. *Physics in Medicine and Biology*, 64(3), 035018. <https://doi.org/10.1088/1361-6560/aafa99>
47. Otsu, N. (1979). A threshold selection method from gray-level histograms. *IEEE Transactions on Systems, Man, and Cybernetics*, 9(1), 62–66. <https://doi.org/10.1109/TSMC.1979.4310076>
48. Lösel, P. D., Van De Kamp, T., Jayme, A., Ershov, A., Faragó, T., Pichler, O., Tan Jerome, N., Aadepu, N., Bremer, S., Chilingaryan, S. A., Heethoff, M., Kopmann, A., Odar, J., Schmelzle, S., Zuber, M., Wittbrodt, J., Baumbach, T., & Heueline, V. (2020). Introducing Biomedisa as an open-source online platform for biomedical image segmentation. *Nature Communications*, 11(1), 5577. <https://doi.org/10.1038/s41467-020-19303-w>
49. Guindon, B., & Zhang, Y. (2017). Application of the dice coefficient to accuracy assessment of object-based image classification. *Canadian Journal of Remote Sensing*, 43(1), 48–61. <https://doi.org/10.1080/07038992.2017.1259557>
50. Setiawan, A. W. (2020). Image segmentation metrics in skin lesion: Accuracy, sensitivity, specificity, dice coefficient, Jaccard index, and Matthews correlation coefficient. In *CENIM 2020 of the Proceeding: International Conference on Computer Engineering, Network, and Intelligent Multimedia 2020* (pp. 97–102). Institute of Electrical and Electronics Engineers Inc. <https://doi.org/10.1109/CENIM51130.2020.9297970>
51. Taha, A. A., & Hanbury, A. (2015). Metrics for evaluating 3D medical image segmentation: Analysis, selection, and tool. *BMC Medical Imaging*, 15(1), 29. <https://doi.org/10.1186/s12880-015-0068-x>
52. Taghanaki, S. A., Liu, Y., Miles, B., & Hamarneh, G. (2017). Geometry-based pectoral muscle segmentation from MLO mammogram views. *IEEE Transactions on Bio-Medical Engineering*, 64(11), 2662–2671. <https://doi.org/10.1109/TBME.2017.2649481>
53. Eelbode, T., Bertels, J., Berman, M., Vandermeulen, D., Maes, F., Bisschops, R., & Blaschko, M. B. (2020). Optimization for medical image segmentation: Theory and practice when evaluating with dice score or Jaccard index. *IEEE Transactions on Medical Imaging*, 39(11), 3679–3690. <https://doi.org/10.1109/TMI.2020.3002417>
54. Terven, J., Cordova-Esparza, D. M., Ramirez-Pedraza, A., & Chavez-Urbiola, E. A. (2023). Loss functions and metrics in deep learning. Published online July 5, 2023. <http://arxiv.org/abs/2307.02694>
55. Ciampiconi, L., Elwood, A., Leonardi, M., Mohamed, A., & Rozza, A. (2023). A survey and taxonomy of loss functions in machine learning. Published online January 13, 2023. <http://arxiv.org/abs/2301.05579>

56. Subramaniam, A., Balasubramanian, P., & Mittal, A. (2018). NCC-Net: Normalized cross correlation based deep matcher with robustness to illumination variations. In *Proceedings of the 2018 IEEE Winter Conference on Applications of Computer Vision, WACV 2018* (pp. 1944–1953). Institute of Electrical and Electronics Engineers Inc. <https://doi.org/10.1109/WACV.2018.00215>
57. Jadon, S. (2020). A survey of loss functions for semantic segmentation. In *2020 IEEE Conference on Computational Intelligence in Bioinformatics and Computational Biology, CIBCB 2020*. Institute of Electrical and Electronics Engineers Inc. <https://doi.org/10.1109/CIBCB48159.2020.9277638>
58. Janocha, K., & Czarnecki, W. M. (2017). On loss functions for deep neural networks in classification. Published online February 18, 2017. <http://arxiv.org/abs/1702.05659>
59. Zhou Wang, Bovik, A. C., Sheikh, H. R., & Simoncelli, E. P. (2004). Image quality assessment: From error visibility to structural similarity. *IEEE Transactions on Image Processing*, 13(4), 600–612. <https://doi.org/10.1109/TIP.2003.819861>
60. Nilsson, J., & Akenine-Möller, T. (2020). Understanding SSIM. Published online June 24, 2020. <http://arxiv.org/abs/2006.13846>
61. You, F., Wu, X., Kelly, M., & Chen, X. (2020). Bioprinting and in vitro characterization of alginate dialdehyde–gelatin hydrogel bio-ink. *Bio-Design and Manufacturing*, 3(1), 48–59. <https://doi.org/10.1007/s42242-020-00058-8>
62. Chen, X. B., Fazel Anvari-Yazdi, A., & Duan, X., Zimmerling, A., Gharraei, R., Sharma, N. K., Sweilem, S., & Ning, L. (2023). Biomaterials /bioinks and extrusion bioprinting. *Bioactive Materials*, 28, 511–536. <https://doi.org/10.1016/j.bioactmat.2023.06.006>
63. Duan, X., Li, N., Chen, X., & Zhu, N. (2021). Characterization of tissue scaffolds using synchrotron radiation microcomputed tomography imaging. *Tissue Engineering Part C: Methods*, 27(11), 573–588. <https://doi.org/10.1089/ten.tec.2021.0155>
64. Izadifar, Z., Honaramooz, A., Wiebe, S., Belev, G., Chen, X., & Chapman, D. (2016). Low-dose phase-based X-ray imaging techniques for in situ soft tissue engineering assessments. *Biomaterials*, 82, 151–167. <https://doi.org/10.1016/j.biomaterials.2015.11.044>
65. Afzal, M. Z., Kolsch, A., Ahmed, S., & Liwicki, M. (2017). Cutting the error by half: Investigation of very deep CNN and advanced training strategies for document image classification. In *2017 14th IAPR International Conference on Document Analysis and Recognition (ICDAR)* (pp. 883–888). IEEE. <https://doi.org/10.1109/ICDAR.2017.149>
66. Duan, X., Fan Ding, X., Khoz, S., Chen, X., & Zhu, N. (2025). Development of a deep learning-based algorithm for high-pitch helical computed tomography imaging. *Expert Systems with Applications*, 262, 125663. <https://doi.org/10.1016/j.eswa.2024.125663>
67. Duan, X., Ding, X. F., Khoz, S., Chen, X., & Zhu, N. (2025). Development of a low-dose strategy for propagation-based imaging helical computed tomography (PBI-HCT): High image quality and reduced radiation dose. *Biomedical Physics & Engineering Express*, 11(1), 015049. <https://doi.org/10.1088/2057-1976/ad9f66>
68. Young, M. L., Rao, R., Almer, J. D., Haefner, D. R., Lewis, J. A., & Dunand, D. C. (2009). Effect of ceramic preform geometry on load partitioning in Al₂O₃-Al composites with three-dimensional periodic architecture. *Materials Science and Engineering: A*, 526(1-2), 190–196. <https://doi.org/10.1016/j.msea.2009.07.033>
69. Helfen, L., Baumbach, T., Stanzick, H., Banhart, J., Elmoutaouakkil, A., & Cloetens, P. (2002). Viewing the early stage of metal foam formation by computed tomography using synchrotron radiation. *Advanced Engineering Materials*, 4, 808–813. [https://doi.org/10.1002/1527-2648\(20021014\)4:10%3C808::AID-ADEM808%3E3.0.CO;2-U](https://doi.org/10.1002/1527-2648(20021014)4:10%3C808::AID-ADEM808%3E3.0.CO;2-U)
70. Sedighi Gilani, M., Boone, M. N., Fife, J. L., Zhao, S., Koebel, M. M., Zimmermann, T., & Tingaut, P. (2016). Structure of cellulose-silica hybrid aerogel at sub-micron scale, studied by synchrotron X-ray tomographic microscopy. *Composites Science and Technology*, 124, 71–80. <https://doi.org/10.1016/j.compscitech.2016.01.013>
71. Li, N., Duan, X., Ding, X. F., Zhu, N., & Chen, X. (2025). Characterization of hydrogel-scaffold mechanical properties and microstructure by using synchrotron propagation-based imaging. *Journal of the Mechanical Behavior of Biomedical Materials*, 163, 106844. <https://doi.org/10.1016/j.jmbbm.2024.106844>
72. Ding, X. F., Zeinali Danalou, S., Zhang, L., & Zhu, N. (2023). In situ wet pharmaceutical granulation captured using synchrotron radiation based dynamic micro-CT. *Journal of Synchrotron Radiation*, 30(Pt 2), 430–439. <https://doi.org/10.1107/S1600577523000826>
73. Blocka, C., Fan Ding, X., Zhu, N., & Zhang, L. (2024). Experimental investigation of dynamic drying in single pharmaceutical granules containing acetaminophen or carbamazepine using synchrotron X-ray micro computed tomography. *International Journal of Pharmaceutics*, 665, 124664. <https://doi.org/10.1016/j.ijpharm.2024.124664>
74. Danalou, S. Z., Ding, X. F., Zhu, N., Emady, H. N., & Zhang, L. (2022). 4D study of liquid binder penetration dynamics in pharmaceutical powders using synchrotron X-ray micro computed tomography. *International Journal of Pharmaceutics*, 627, 122192. <https://doi.org/10.1016/j.ijpharm.2022.122192>

How to cite this article: Ding, X. F., Duan, X., Li, N., Khoz, Z., Wu, F.-X., Chen, X., & Zhu, N. (2025). Development of a deep learning method for phase retrieval image enhancement in phase contrast microcomputed tomography. *Journal of Microscopy*, 1–16. <https://doi.org/10.1111/jmi.13419>